
Article:
Arnold, N.S. and Butcher, F.E.G. orcid.org/0000-0002-5392-7286 (2026) Estimating the age of ice in a Martian mid-latitude debris-covered glacier from numerical modelling and particle tracking. Icarus, 444. 116839. ISSN: 0019-1035

https://doi.org/10.1016/j.icarus.2025.116839

Icarus 444 (2026) 116839

Contents lists available at ScienceDirect

Icarus

journal homepage: www.elsevier.com/locate/icarus

Research Paper

Estimating the age of ice in a Martian mid-latitude debris-covered glacier from numerical modelling and particle tracking☆

N.S. Arnold [a,*], F.E.G. Butcher [b]

[a] Scott Polar Research Institute, University of Cambridge, Lensfield Road, Cambridge CB2 1ER, UK
[b] School of Geography and Planning, University of Sheffield, Sheffield S10 2TN, UK

ARTICLE INFO

Keywords:
Mars glaciation
Mars missions
Ice flow modelling
Particle tracking
Ice age

ABSTRACT

Mars' mid latitudes contain thousands of 'viscous flow features' (VFFs), akin to debris-covered glaciers on Earth. They are thought to have formed during martian 'ice ages', driven by variations in Mars' spin-axis obliquity. Knowledge of the emplacement age of ice within VFFs is key to understanding the nature and timing of such glacial cycles, and the palaeoclimate histories they reflect. Current methods to estimate VFF surface ages, which place VFF formation broadly within the last few Myr to 100 s Myr, predominantly rely on the size-frequency distributions of impact craters across their surfaces. However, these 'impact crater retention ages' likely reflect the time since the emplacement or last major modification of the surficial debris layer; they implicitly assume a uniform age across the sampled area. They also provide no direct information about the emplacement ages of the underlying ice layers, the configurations (and hence age distributions) of which are likely to have been modified during transit by ice flow. Here, we develop a new, physically-based method to reconstruct the flow paths and transit times of ice within VFFs, and hence estimate variations in the minimum age of ice across their (now debris-covered) surfaces, and with depth. We use 3-dimensional ice flow modelling and particle tracking, and apply our method to a small VFF in Mars' southern mid-latitudes, north of Argyre Planitia. Our method produces spatially-variable near-surface ice age estimates which range from very young (< 1Myr) in the upper parts of the VFF to ~500 Myr close to the VFF terminus, assuming current martian temperatures and a conventional ice rheology. Toward the terminus, the calculated surface ages increase rapidly over short distances as compressional ice flow transports old, deep ice upwards toward the surface. The distributed 3D age estimates provided by our method also allow prediction of the depths and configurations of isochronous layers within the VFF. The spatial patterns we find are insensitive to the assumed ice deformation mechanism, but the specific calculated ages are highly sensitive (> 2 orders of magnitude) to ice temperature and grain size, which emerge as the main controls on modelled ice flow velocities, and hence the estimated ages. Our results have significant implications for identifying landing sites and ice sampling strategies for future missions which could extract climate records potentially hosted within glacial ice layers on Mars. The significant variations we find in the age of ice across the VFF surface, arising from the flow-induced deflection of ice layers up to the surface, suggest that such missions could access ice with a large range of ages (and hence potentially longer-timespan climate records) by sampling from shallow depths across the surface a single VFF.

1. Introduction

1.1. Background

Thousands of 'viscous flow features' (VFFs) in Mars' mid latitudes (Fig. 1), akin to debris-covered glaciers on Earth (Holt et al., 2008; Plaut et al., 2009; Souness et al., 2012; Petersen et al., 2018), are thought to have formed in the last several Myr to 100 s Myr (e.g. Baker and Carter, 2019; Hepburn et al., 2020; Berman et al., 2021), when orbitally-forced climate cycles permitted mid-latitude ice accumulation (Laskar et al., 2004; Madeleine et al., 2009). VFFs are not accumulating ice in the present day; the ice within VFFs is a relict of past climate, preserved beneath a protective layer of surficial dust and debris (Holt et al., 2008; Plaut et al., 2009). VFFs and other mid-latitude ice deposits on Mars are

☆ This article is part of a Special issue entitled: 'Mars Polar Science' published in Icarus.

* Corresponding author.
E-mail addresses: nsa12@cam.ac (N.S. Arnold), f.butcher@sheffield.ac.uk (F.E.G. Butcher).

https://doi.org/10.1016/j.icarus.2025.116839
Received 25 April 2025; Received in revised form 22 August 2025; Accepted 1 October 2025
Available online 2 October 2025

therefore key indicators of recent planetary-scale climate changes. They have also emerged as key targets for future missions aiming to access mid-latitude ice on Mars (e.g. Morgan et al., 2025; Morgan et al., 2021). This includes, for example, the ice-drilling 'Mars Life Explorer' lander concept (Williams, 2021; National Academies of Sciences, 2023), and eventual human missions (Mars Ice Core Working Group, 2021; I-MIM MDT, 2022), which could extract records of past climate changes in ice cores (Mars Ice Core Working Group, 2021). Knowledge of the age of ice within VFFs, and its variations both spatially and with depth, is critical for deciphering from orbit the palaeoclimate histories recorded by VFFs,

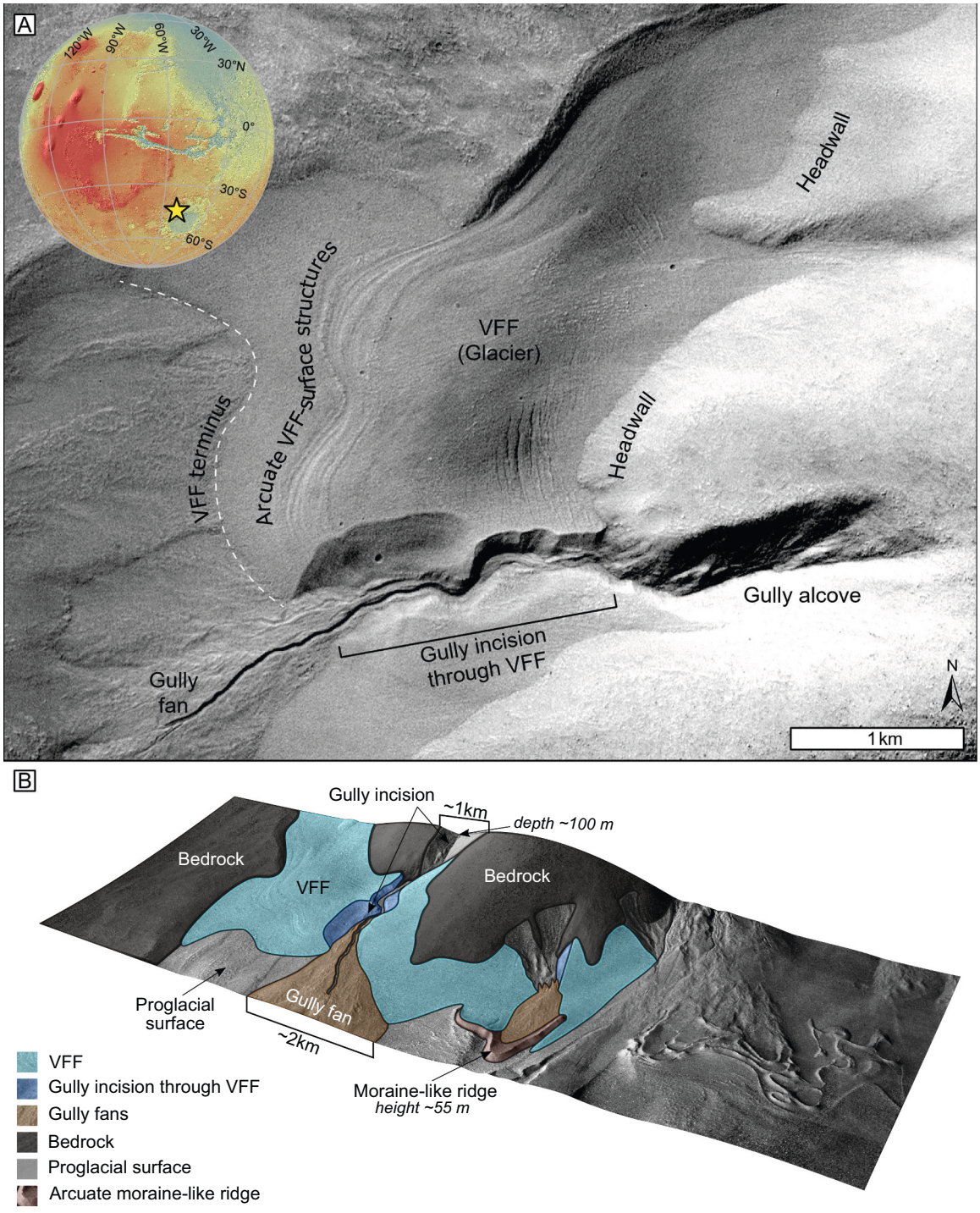

Fig. 1. A small VFF (a putative debris-covered glacier) in Nereidum Montes (51.24°W, 42.53°S), the subject of this study and a previous study by Butcher et al. (2024). (A) 6 m/pixel Context Camera (CTX; Malin et al., 2007) image P14_006572_1367_XN_43S051W showing the VFF (terminating at the white dashed line), and the major arcuate VFF-surface structures cut through by a gully, as described by Butcher et al. (2024). The inset Mars Orbiter Laser Altimeter (MOLA; Smith et al., 2001) elevation map of Mars shows the location of Nereidum Montes. (B) Oblique view of the VFF overlain by a schematic map identifying key landscape features. The base image is an orthorectified 25 cm/pixel High Resolution Imaging Science Experiment (HiRISE; McEwen et al., 2007) image, ESP_051036_1370, overlain on a 1 m/pixel HiRISE digital terrain model (DTM; see Data Availability). Modified from Butcher et al. (2024). CTX data credit: NASA/JPL/MSSS/UfoA. MOLA data credit: USGS Astrogeology Science Center/Goddard Space Flight Center/NASA. HiRISE data credit: NASA/JPL/University of Arizona/NHM.

and for identifying the most scientifically valuable landing sites and sampling strategies for future ice-sampling missions.

Currently, the ages of VFFs are often estimated by analysing the size-frequency distributions of impact craters on their surfaces (e.g. Baker and Carter, 2019; Hepburn et al., 2020; Berman et al., 2021). However, impact crater retention ages more closely reflect the time since the last major modification of the surficial debris layer hosting counted impact craters. Impact crater retention ages for VFF surfaces therefore very likely underestimate the true age of ice beneath the surface debris layer (Baker and Carter, 2019), which likely differs in age from the surface debris layer.

It is possible to employ crater counting approaches to bracket the broad time period within which VFFs likely formed by analysing impact crater populations on geologic units which underlie (and hence predate) and – more rarely - overlie (and hence post-date) VFFs in the stratigraphy. Such analyses demonstrate with high confidence that VFFs are indeed geologically young (in a martian context; they are generally > 100 times older than any terrestrial glacier), likely having formed within the last ~1 Gyr, i.e., during the mid-to-late Amazonian period (e.g. Tanaka et al., 2014; Butcher et al., 2021; Woodley et al., 2022), with some VFFs having formed within the last several million to 100 s Myr (e.g. Fassett et al., 2014; Conway et al., 2018; Hepburn et al., 2020).

Some previous numerical modelling studies have attempted to constrain the timespan required to form glaciers with similar extents, thicknesses, and surface profiles to VFFs. For example, focussing on small kilometre-scale VFFs, Milliken et al. (2003) used the composite flow law of Goldsby and Kohlstedt (2001) to find that, under the most likely temperature and ice grain size scenarios for Mars, VFFs could form over periods of several tens of Myr. In a later study, focussing on a ~ 10 km-long, several hundred m-thick VFF in Euripus Mons, Parsons and Holt (2016) found that realistic VFF profiles were produced by a period of rapid precipitation lasting less than 1 Myr at high elevations, followed by a period of viscous relaxation. The timescale required for the model profiles to match the observed VFF profiles varied by orders of magnitude, from tens to hundreds of Myr, depending on the specific model parameters (i.e. temperature, ice grain size and ice dust content) and form of the ice flow law chosen.

Such modelling studies have proven extremely valuable in broadly corroborating the results of impact crater retention age approaches, confirming that VFFs could indeed have formed within the last few million to hundreds of millions of years. However, the problem remains that existing methods provide no information on the 3-dimensional variations across and within VFFs. These age distributions will be affected by lateral and vertical variations in ice flow vectors, and are critical to deciphering the palaeoclimate histories VFFs record.

1.2. *Effects of ice flow on the age distribution of ice within glaciers*

In typical terrestrial glacial systems, ice flows both horizontally, along the direction of flow (typically the direction of the steepest surface slope), and vertically, into or out of the body of the glacier (Fig. 2). Accumulation of snow at higher elevations leads to burial, and hence to the age of ice layers increasing with depth (Fig. 2). At lower elevations, ablation leads to exposure of sequences of deeper, older ice layers at the surface (Fig. 2); on Earth ablation typically occurs via melting, but sublimation (likely the dominant ablation process on Amazonian Mars) can also play an important role in ice loss, especially in cold, dry, windy areas of Antarctica (e.g. Frezzotti et al., 2004; Scambos et al., 2012; Das et al., 2013).

Importantly, vertical ice movement also occurs independently of the surface mass balance, driven by the horizontal flow of ice as it moves downhill due to gravity. Extensional flow (typical in the upper parts of glaciers and ice sheets) leads to downwards vertical movement of ice, transporting younger ice from the surface into the body of the glacier; compressive flow (typical at lower elevations) leads to upwards vertical flow, bringing older, deeper ice back up toward the surface (Fig. 2).

The influence of ice flow on the distribution of ice of different ages within glaciers motivates us to develop a numerical modelling approach by which intra-VFF age variations can be evaluated.

Under contemporary mid-latitude climate conditions on Mars, VFFs are not thought to be accumulating ice, and their surfaces are completely covered by dust and/or debris. Uncertainty exists over the specific role of the surficial debris cover in the long-term evolution of different VFFs. However, SHARAD (SHAllow RADar) orbital radar evidence from hundreds of large (100 s m thick) VFFs reveals high ice volume percentages, surficial debris thicknesses of <~10 m, and a paucity of detectable

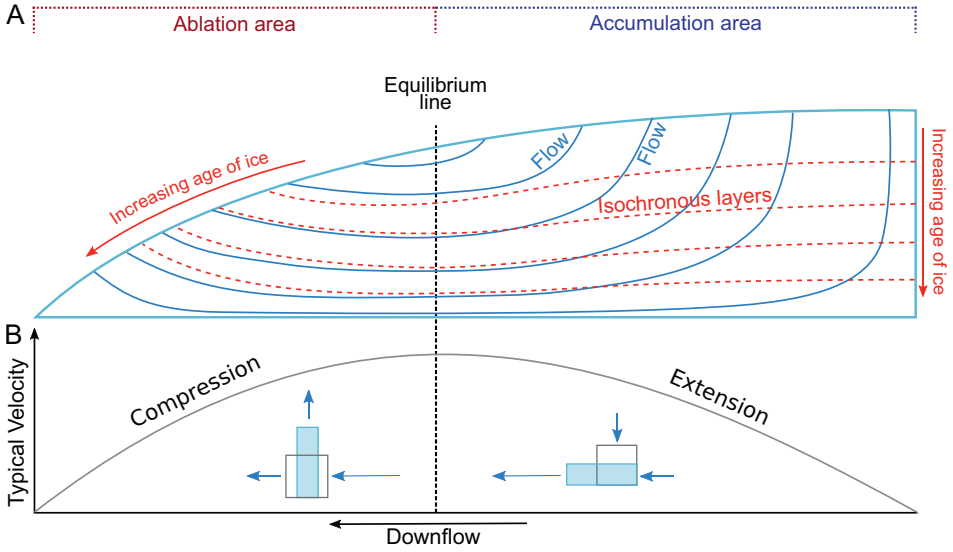

Fig. 2. (A) Schematic showing typical flow paths (blue lines) through a glacier and resulting configuration of isochronous ice layers (red dashed lines) with respect to the surface. The accumulation zone is in the upper (right) part of the glacier, and the ablation zone in the lower (left) part. The equilibrium line is at the elevation where accumulation approximately balances ablation. Modified from Jennings and Hambrey (2021), after Hooke and Hudleston (1978). (B) Schematic representaton of the typical variations in ice flow velocity along a glacier flowline (grey curve), and resulting horizontal and vertical deformation of parcels of ice (boxes, with blue arrows representing horizontal and vertical velocity magnitudes - not to scale). (For interpretation of the references to colour in this figure legend, the reader is referred to the web version of this article.)

internal debris layers (e.g. Holt et al., 2008; Plaut et al., 2009; Petersen et al., 2018). This implies that many VFFs may have accumulated as clean-ice glaciers and that their surficial dust and/or debris cover potentially accumulated after the major period(s) of ice accumulation. While orbital radar data is unable to resolve similar information for small, kilometre-scale VFFs, or VFFs in topographically complex settings, it seems likely that many such features evolved in a similar manner to larger VFFs. However, as on Earth, a continuum of glacier debris concentrations likely exists on Mars (from clean ice glaciers through debris-covered glaciers to rock glaciers, e.g. Anderson et al., 2018), and some VFFs may have evolved as continually debris-covered or rock glaciers (e.g. Levy et al., 2021).

Among terrestrial glaciers, the relative sizes of the accumulation and ablation areas, and hence the specific position of the equilibrium line (Fig. 2), varies enormously, including between glaciers with different thickness and extents of surficial debris cover, and under different climatic regimes. Such variations would alter the local patterns of horizontal and vertical movement, but the general principles of expected bulk flow illustrated in Fig. 2 still apply. In the present study, we predominantly focus on the clean-ice glacier scenario for VFF evolution, but explore the potential impact of (well-mixed) englacial lithic fractions of up to 16 %.

1.3. Ice flow and access to palaeoclimate records in ice samples/cores

Understanding variations in the age of ice within individual VFFs has important implications for interpreting the palaeoclimate records provided by VFFs from orbit and for planning future missions to sample the ice.

Records of past climate and environmental change can be extracted from glaciers and ice sheets in ice cores, which host these records in sequences of ice layers deposited through time. Traditional approaches to ice coring on Earth access ice age sequences by coring vertically through sub-horizontal layers, typically high in the accumulation zone where primary ice layers are usually best preserved; deeper cores are required to reach older ice layers. Significant scientific effort has been invested, and continues to be invested, in terrestrial glaciological studies searching for candidate ice coring sites on Earth which host the oldest ice and hence the longest possible palaeoclimate records (e.g. Fischer et al., 2013).

VFFs have thicknesses ranging from several 10s to 100 s of metres (e.g. Milliken et al., 2003; Holt et al., 2008; Plaut et al., 2009; Butcher et al., 2024). An initial assessment of the scientific potential of martian ice cores worked with an assumption of a 20 m vertical coring depth (Mars Ice Core Working Group, 2021). Under a traditional vertical ice coring approach this would provide access to the shallowest ice layers and hence the youngest portion of the climate records within VFFs. However, this does not necessarily mean that older ice would be inaccessible. As explained above, and shown in Fig. 2, ice flow can bring deeper, older ice to glacier surfaces, particularly near to their termini, with the age of ice at the surface increasing toward the ice terminus (Schaefer et al., 2009; MacGregor et al., 2020).

Given the theoretical flow patterns shown in Fig. 2, shallow samples taken near to VFF termini should allow access to old ice (Butcher et al., 2024); at the time of writing, the oldest ice extracted from an ice core on Earth – dated to 4.6 Myr – was sampled from ice transported by ice flow up to the surface near to the coast of Antarctica (Brook and Center for Oldest Ice Exploration Allan Hills Research Team, 2025), although complex flow has led to discontinuous age sequences of ice in this region. “Horizontal ice coring” in marginal areas of the Greenland Ice Sheet has produced near-continuous climate records extending back several tens of thousands of years into the last glacial period, which broadly match records from vertical ice cores (Schaefer et al., 2009; MacGregor et al., 2020). Hence, while vertical ice coring is the “gold-standard” approach for extracting climate records from glacial ice, multiple shallow samples taken along a traverse from VFF terminus to VFF interior could provide age sequences of old ice. Horizontal ice coring approaches could complement vertical ice coring on martian VFFs to extend the age range of accessed ice, and hence the potential timespans of extractable climate records.

1.4. Approach and study site

Here, we develop a new, physically-based methodology using a combination of numerical ice flow modelling and particle tracking to estimate the age of ice within and across a VFF, based on ice flow physics, for a range of different assumed surface temperatures and ice flow parameters.

We apply our method to a small VFF in the Nereidum Montes region of Mars’ southern mid-latitudes (51.24°W, 42.53°S, Fig. 1; Butcher et al., 2024), to the north of Argyre Planitia. Impact crater retention ages for the surfaces of similar VFFs in the region are ~2.7 Myr (Berman et al., 2021). The VFF (Fig. 1) was the subject of our recent study (Butcher et al., 2024), summarized in Fig. 3, which identified VFF-internal layering exposed in the wall of a gully which incises through the VFF (Fig. 1, 3 A). Butcher et al. (2024) demonstrated that the layers become more inclined down-flow (Fig. 3B, C), matching theoretical flow paths (Fig. 2), and connecting to arcuate VFF-surface structures near the VFF terminus (Fig. 3A, B). This is reminiscent of layer configurations at the snouts of many terrestrial glaciers. Ice flow modelling in Butcher et al. (2024) study showed that modelled ice-flow vectors become increasingly oriented toward the ice surface approaching the VFF terminus due to along-flow ice compression. This deflection of ice-flow vectors correlates with the area of the outcropping layers and surface structures (Fig. 3D; Butcher et al., 2024). Butcher et al. (2024) suggest that these dipping structures could represent ice layers (and potentially intervening dust/debris bands) that have been transported up to the surface from deep interior positions by ice flow.

Given theoretical ice flow paths, observations of inclined layers intersecting VFF-surface structures on Mars, and the potential for future missions to extract climate records from VFFs in ice cores/samples, the age of the ice within VFFs, and its horizonal and vertical variations, become critical questions. In this study, we therefore extend our previous modelling experiments (Butcher et al., 2024) to demonstrate a new method for providing physically-based and spatially-variable estimates of the transit time of ice through VFFs and the resulting 3D variations in the age of ice within VFFs. We explore modelled variations in the age of the near-surface ice across the VFF, and at different depths through the ice column, and investigate the effect of climate (through mean annual surface temperature), ice dust content, and assumed dominant ice flow mechanism on the calculated age distributions. We assume a steady-state VFF morphology, meaning the resulting spatial variations in ice transit times are minimum ages. We defer the possible effects of multiple phases of ice accumulation, for example due to obliquity-driven climate cycles (e.g. Levy et al., 2021), to future developments of the method.

2. Methods

To simulate VFF flow, we used a 3-dimensional, high-order ice flow model, ISSM, (Larour et al., 2012) with a HiRISE-derived surface DTM (Fig. 4A) and an inferred bed topography. We derived the bed topography using natural neighbour interpolation from the elevations of the upstream and downstream VFF margins, and the elevation along the base of gully that incises through the VFF (Butcher et al., 2024). Here, we additionally assume that the hollow on the ice surface containing visible crevasses (north of the gully, and just downstream of the headwall) results from a hollow in the bedrock. We simulate this by assuming the ice thickness is constant along 5 additional lines of points running north from the gully edge, sub-parallel with the VFF headwall (Fig. 4B); the ice thickness along each line was taken as the ice thickness measured at the gully wall at the start point of each line.

Ice flows as a viscous material under an applied stress, where the rate

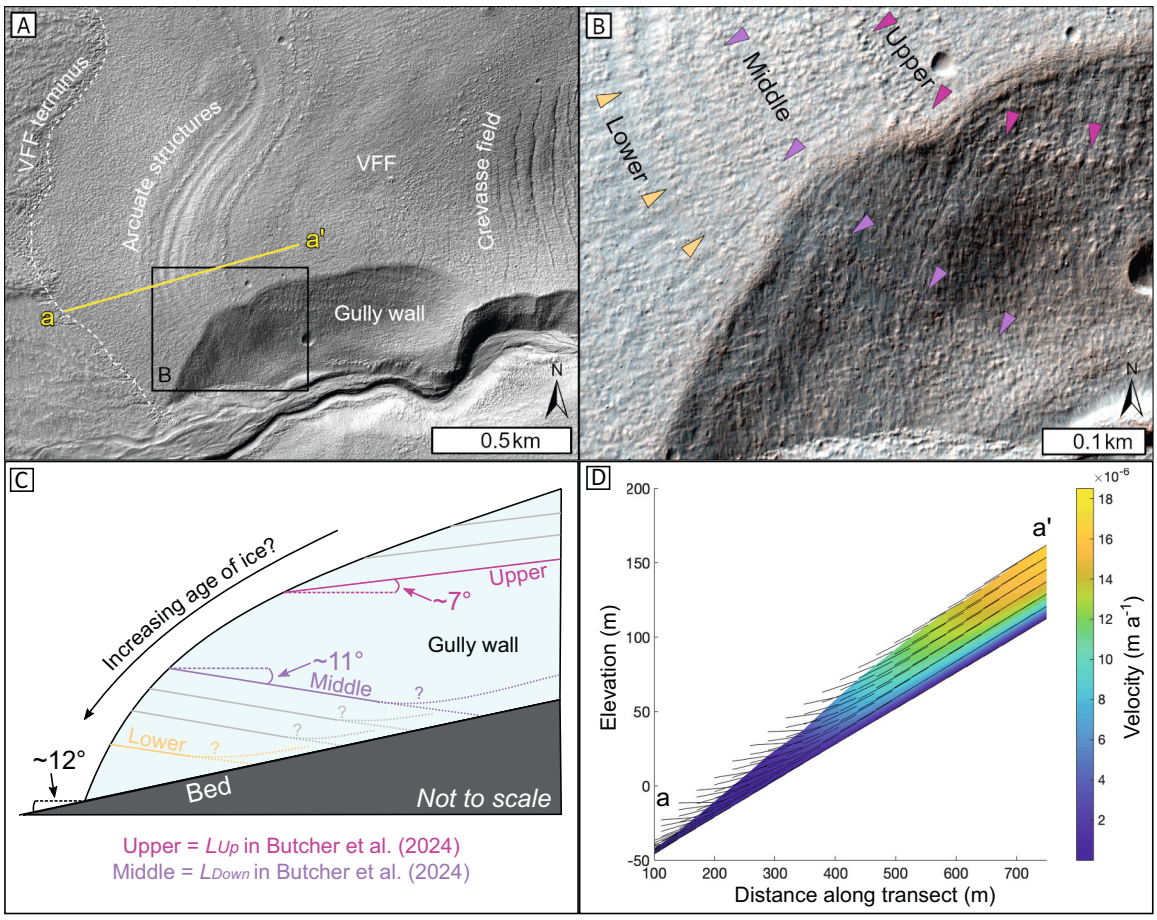

Fig. 3. Relationship observed by Butcher et al. (2024) between major arcuate surface structures on the VFF, and tilted layers in the wall of the gully. The tilted layers and arcuate surface structures occur where ice flow modelling performed in that study predicted upwards deflection of ice flow vectors. (A) Orthorectified HiRISE image ESP_051036_1370_RED showing the intersection between the arcuate surface structures and the gully wall, as well as the extent of panel B and the approximate location of transect a-a' in panel D. (B) HiRISE false-colour image ESP_051036_1370_MRGB showing the colour signatures of layers in the gully wall which connect to the arcuate surface structures. Three major surface structures termed 'Upper', 'Middle', and 'Lower' in the present study are labelled. Butcher et al. (2024) refer to Upper as 'L_{Up}', and Middle as 'L_{Down}'. (C) Schematic (not to scale) showing the dip angles measured by Butcher et al. (2024) for the VFF-internal layers connecting to the Upper and Middle arcuate surface structures, and the slope of the bed at the VFF terminus. The black arrow illustrates the hypothesis explored in the present study, that if the layers connecting to the arcuate surface structures have become upwarped by ice flow, ice layers outcropping nearer to the terminus likely source from deeper, older layers. Modified from Butcher et al. (2024). (D) The modelled ice flow velocity profile from Butcher et al. (2024) showing the deceleration of ice toward the terminus, and the deflection of velocity vectors (black feathers of uniform length show the orientation of the x,z component of velocity) up toward the surface. Elevations are from the HiRISE DTM used in their model. Modified from Butcher et al. (2024). HiRISE data credit: NASA/JPL/University of Arizona/NHM.

of deformation depends non-linearly on the applied stress, the ice hardness, and the ice grain size (e.g. Glen, 1955; Goldsby and Kohlstedt, 2001; Cuffey and Paterson, 2010; Schmidt et al., 2019):

$$\dot{\varepsilon} = A\tau^{n}d^{-p}, \tag{1}$$

where $\dot{\varepsilon}$ is the strain rate, τ is the applied stress, A is the ice hardness or rigidity, d is the ice grain size, n is the ice flow exponent, and p the grain size exponent. The flow exponent, n, has been found to vary between 1 and 4.2 (Goldsby and Kohlstedt, 2001) depending on the specific deformation mechanism involved. In general, glacier ice on Earth and Mars is thought to flow by a combination of grain-size-sensitive creep (gss, also known as super-plastic flow; Goldsby and Kohlstedt, 2001; Schmidt et al., 2019) for ~10 kPa $< \tau <$ ~100 kPa, where $n = 1.8$, and dislocation creep for $\tau >$ ~100 kPa, where $n = 4$. Thus, $n = 3$ has emerged as a "happy compromise" between the two main flow mechanisms at typical glacial stress values and is by far the widest adopted value in the literature, and is also the most consistent with (terrestrial) field data (Cuffey and Paterson, 2010). The grain size exponent, p, also varies with the flow mechanism. For gss creep, $p = 1.4$, but dislocation creep is unaffected by grain size, as $p = 0$ (Goldsby and Kohlstedt, 2001).

The ice hardness, A, is strongly affected by temperature (among many other factors, including hydrostatic pressure, density, water content and other impurities, and ice fabric orientation (Cuffey and Paterson, 2010)), typically following an Arrhenius relationship (Cuffey and Paterson, 2010):

$$A = A_0 \exp\left(\frac{-Q + PV}{RT}\right) \tag{2}$$

Here, A_0 is the temperature-independent flow factor, Q is the activation energy, P is the pressure, V is the activation volume for creep, R is the gas constant and T is the absolute temperature. A_0, Q and V vary with the flow mechanism. Model parameters and constants are given in Table 1.

Gravity pulls glaciers vertically downward. This vertical force then causes horizontal flow of ice as it sets up pressure gradients within the glacier due to spatial variations in ice thickness, and because the glacier may rest on a sloping bed (Cuffey and Paterson, 2010). The gravitational driving stress, τ_d is calculated as

$$\tau_d = \rho g H tan(\alpha), \tag{3}$$

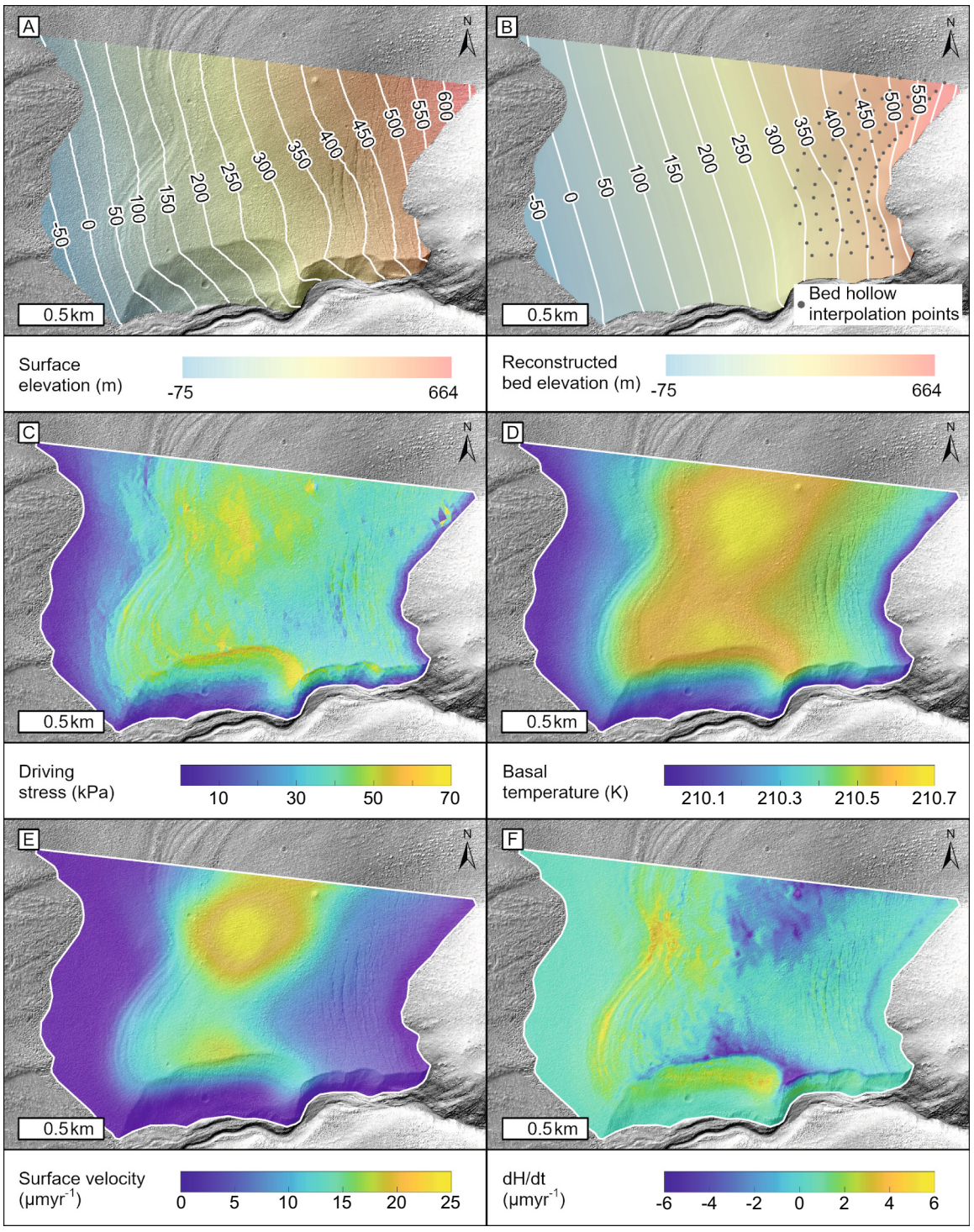

Fig. 4. First-order controls on ice flow in transient model runs performed in this study. Panels A and B show key model inputs, and Panels C—F show key results for the standard model run ($n = 3$, $T_s = 210$ K). The basemap for all panels is orthorectified HiRISE image ESP_051036_1370_RED. (A) Elevation of the VFF surface within the model domain, derived from the HiRISE DTM generated by Butcher et al. (2024; see Data Availability). White lines show surface elevation contours at 50 m elevation intervals. (B) Reconstructed elevation of the VFF bed, overlain on a shaded relief map of the reconstructed bed. Grey points show the locations of a set of 'bed hollow interpolation points' with elevations set to approximate a hollow in the bed inferred on the basis of the observed depression in the VFF surface near to the headwall (see Methods for bed reconstruction approach). White lines show reconstructed bed elevation contours at 50 m elevation intervals. (C) Modelled gravitational driving stress. (D) Modelled basal ice temperature. (E) Modelled ice surface velocity. (F) Modelled ice thickness (H) change due to flow convergence/divergence, the negative of which is used as the SEC to maintain a steady-state VFF morphology in time-dependent model runs (see Methods). HiRISE data credit: NASA/JPL/University of Arizona/NHM.

Table 1
Model parameter values.

Parameter	Symbol	Value	Source
Gravity	g	3.711 ms^{-2}	(standard)
Ice density	ρ_i	917 kgm^{-3}	(standard)
Dust density	ρ_d	3000 kgm^{-3}	a
Temperature-invariant ice hardness	A_0	3.9×10^{-15} $Pa^{-n}s^{-1}$	b, c
Activation energy	Q	49,000 $Jmol^{-1}$	a, b, c
Volume creep activation energy	V	-1.3×10^5 m^3mol^{-1}	c
Gas constant	R	8.314 $Jmol^{-1}$ K^{-1}	(standard)
Dust particle size	–	100 μm	a
Surface temperature	Ts	200 K – 230 K	(sensitivity)
Ice grain size	d	0.5 mm – 5 mm	(sensitivity)
Ice flow exponent	n	2, 3	(sensitivity)
Grain size exponent	p	1.4 (n = 2); 0 (n = 3)	(sensitivity)

a. Parsons and Holt (2016)
b. Goldsby and Kohlstedt (2001)
c. Schmidt et al. (2019)
(standard) indicates physical constants or assumed standard values.
(sensitivity) indicates parameters varied in the model experiments.

where ρ is the material density, g is gravity, H is the ice thickness and α is the surface slope. The gravitational driving stress is ultimately balanced by a set of resistive stresses within, and at the base (and edges) of an ice mass. A simplifying assumption, which we do not use, but is widely used in earlier terrestrial modelling studies as well as modelling studies of martian VFFs (e.g. Parsons and Holt, 2016; Schmidt et al., 2019; Fastook and Head, 2024), is that τ_d is the dominant stress, and is only balanced by the friction at the base of the glacier (Cuffey and Paterson, 2010). This simplification is part of the so-called "shallow ice approximation" (SIA, Hutter, 1983). The SIA neglects other stresses such as longitudinal stretching or compression and hence their role in vertical ice movement (Fig. 2), and transverse stresses such as drag against valley sides. These stresses become increasingly dominant toward the terminal and lateral margins of ice masses. SIA models are also often vertically-integrated, and so neglect possible vertical ice flow within the body of the ice. Over the last 10–15 years, terrestrial ice sheet modelling has seen the development of so-called "higher order" ice sheet models which incorporate these additional stress components in a variety of ways (e.g. Hanna et al., 2013) to address the simplifications of the SIA, allowing more accurate calculations of internal flow fields within ice masses.

Here, given we are specifically interested in flow within the body of a VFF, ISSM (Larour et al., 2012), as a higher-order model, allows us to specifically model the vertical as well as horizontal movement of ice, and the impact of longitudinal and lateral stress throughout the VFF, but especially near the ice margins. ISSM can calculate the full Stokes equations for flow, but here we adopt the implementation within ISSM of the Blatter-Pattyn approximation (Blatter, 1995; Pattyn, 2003) to the Stokes equations. This approximation assumes that the vertical component of the momentum balance is hydrostatic (and hence buoyancy forces are zero) and that horizontal gradients in vertical velocity are small compared to the vertical gradient in the horizontal velocity (see, for example, Rückamp et al. (2022) for a useful summary). It still allows the full 3-dimensional stress and velocity fields to be calculated, but leads to a significant saving in computational expense with negligible impact on model results given the very slow ice flow velocities typical for Mars (Arnold et al., 2022). In all runs, the VFF was assumed to be frozen to its bed, with zero basal velocity.

Given the ongoing uncertainty around the controlling processes for martian ice flow (e.g. Milliken et al., 2003; Parsons et al., 2011; Karlsson et al., 2015; Parsons and Holt, 2016; Schmidt et al., 2019), and therefore in appropriate values for n, p and d, we conducted a range of model experiments with $n = 3$ and $n = 2$ to simulate flow by a combination of dislocation creep and gss creep, or "pure" gss creep, with a range of assumed surface temperatures and, in the case of the $n = 2$ runs, ice grain sizes.

For runs with $n = 3$, we varied the assumed mean annual surface temperature (T_s, currently ~210 K at ~40°S (Millour et al., 2018)) in 5 K increments from 200 K to 230 K, calculating A using the temperature parameterization implemented in ISSM, which is based on that in Cuffey and Paterson (2010), and which follows an Arrhenius relationship as for Eq. 2. Flow is assumed to be independent of grain size (i.e. $p = 0$ in Eq. 1) in the $n = 3$ runs. In the subsequent discussion, we treat the $n = 3$, $T_s =$ 210 K run as the standard run.

For runs with $n = 2$ and $p = 1.4$, we assume a surface temperature of 210 K, calculating A using Eq. 2 and the parameters in Table 1. We vary d from 0.5 mm to 5 mm, the range of sizes investigated by Parsons and Holt (2016) in a study of a VFF at Euripus Mons. For these runs, the assumed ice grain size is thought to depend on the dust content of the ice, as dust limits ice grain size (Barr and Milkovich, 2008). Given that we fix the grain size, we calculate the inferred dust volume concentration, ϕ, as:

$$\phi = \left[\left(\frac{0.002}{d}\right)^2\right] \Big/ 100 \tag{4}$$

(adapted from Barr and Milkovich, 2008; Parsons and Holt, 2016), assuming a dust particle size of 100 μm (Parsons and Holt, 2016; Schmidt et al., 2019). The dust volume concentration varies from 16 % for $d = 0.5$ mm to 0.16 % for $d = 5$ mm; we calculate the resulting bulk density of the VFF (ρ) as:

$$\rho = (1 - \phi)\rho_i + \phi\rho_d \tag{5}$$

where ρ_i is the ice density, and ρ_d is the dust density, following Parsons and Holt (2016). Varying dust content therefore affects the modelled stresses within the ice mass via the gravitational driving stress, τ_d, (Eq. 3) in the $n = 2$ experiments.

For all model runs, following Butcher et al. (2024), the model was initialized to a thermomechanically coupled, stress-balanced steady state (to allow for the impact of strain heating on ice flow, Butcher et al., 2017) using the assumed mean annual surface temperature and grain size. Initial experiments showed that varying the geothermal heat flux between 20 mWm^{-2} and 50 mWm^{-2} made less than 6 % difference in the estimated surface ice age in the area of the surface structures (our key area of interest, with the largest calculated ages) for the standard run; therefore, for all runs we used a geothermal heat flux of 30 mWm^{-2} (Sori and Bramson, 2019).

We assume the VFF accumulated some time in the past as relatively pure ice, with any lithic fraction evenly distributed, and we assume a steady-state VFF morphology. The stress-balance runs therefore give an instantaneous picture of ice flow within the VFF. However, the calculated spatial variations in ice flow they produce would drive ice thickness changes over time. Thus, to maintain a steady state morphology over time-dependent runs, we then ran ISSM in time-dependent mode with zero surface mass balance to calculate the ice thickness change due to ice flow in one model time step (1 Earth year). Following Arnold et al. (2022), we then used the negative of this change as an assumed surface elevation correction (SEC) for the duration of the transient model runs. Areas with modelled surface lowering are therefore balanced by a positive SEC, and vice versa, with the sum of the SEC term across the VFF being zero. This approach minimizes the change in VFF morphology due to ice flow, creating a long-term "steady state" (though not static) VFF.

The final stage in all experiments was a 5 Myr-duration transient run. This duration is somewhat arbitrary, as the modelled VFF morphology and flow velocity do not change during the run; using 5 Myr allowed us to check for numerical stability, and that the SEC term applied did indeed give a stable VFF morphology throughout each run.

We next sought to assess the theoretical 'transit time' required for particles to be transported through the VFF by ice flow to different positions across the ice surface and through the ice column. These transit times form first-order estimates of the minimum age of the ice. We

calculated particle paths using a forward Euler scheme implemented in the MATLAB® programming language. Seed particles were positioned across the surface of the VFF and their implied movement tracked downstream using the 3-dimensional velocity vector field calculated by ISSM. For each particle path, the tracking algorithm stopped when the particle emerged onto the VFF surface, or if the path touched the bed, or where the path crossed the lateral margins of the VFF (taken to be locations with $H < 1$ m, due to the negligible stresses in these areas, and hence extremely slow modelled ice velocities $<1 \times 10^{-9}$ m yr^{-1}). Given our assumption of a frozen bed, no paths touched the bed. We used a dense mesh of 4860 seed particles to calculate the surface and internal age distribution within the model domain, with particles placed on a 25 m grid across the VFF surface, with a randomized gaussian "jitter" (up to ±6.25 m) to reduce any possible effects of completely regular particle spacing. We integrated ice velocities along the reconstructed particle paths to give the transit time between deposition and re-emergence at the surface.

Given our assumption of steady state VFF morphology and ice flow, the calculated transit times assume constant ice velocities throughout particle transport, but they represent first-order physically-based estimates of the age distribution of ice under a stable climate and ice-flow regime. We therefore took the total transport duration along each particle path as an estimate of the minimum age of ice at each point where modelled particle paths emerge onto the VFF surface in the model, allowing spatial variations in the surface age to be approximated across the VFF. In reality, ice in VFFs is buried by a thin layer of dust and/or debris, but given typical particle path lengths we calculate, especially to areas in the vicinity of the arcuate surface structures, the ~1–10 m estimated debris thickness for VFFs (e.g. Holt et al., 2008) makes << 1 % difference to calculated ice ages so the effect of any debris cover thickness was ignored. Our estimated ages can therefore be taken strictly as the minimum age of the ice immediately underneath any surface debris cover, rather than the age of any debris cover at the surface itself. The particles were placed with an initial age of zero; the algorithm stored the incrementally-increasing ages and positions at each step along each particle path, allowing the age of ice to be calculated at different depths throughout the VFF interior. We also tracked specific particles emerging at 21 locations along the arcuate surface features identified by Butcher et al. (2024) (Figs. 1 A, 3 A) as connecting to visible internal layers, to highlight particle flow paths to those structures.

3. Results

Fig. 4 shows the VFF surface (Fig. 4A) and bed (Fig. 4B) morphology used in all model runs, together with the first-order controls on the ice flow resulting from the VFF morphology. In the standard run, gravitational driving stress (Fig. 4C, Eq. 3) averages around 40–60 kPa, despite Mars' lower gravity. It increases in the $n = 2$ runs, by up to ~30 % for the $d = 0.5$ mm run because of the higher bulk VFF density due to dust (Eq. 5). These values are within the range of "typical" values for terrestrial glaciers, albeit at the lower end of this range; for this specific VFF, they result from the steep surface slope rather than the thickness of the ice. The small thickness of the VFF (maximum thickness ~ 50 m) allows geothermal heat and any strain heating to be conducted to the cold ice surface easily; hence, calculated basal heating is small, reaching a maximum of ~0.75 K in the standard run (Fig. 4D), and is less than 1 K in all other runs.

As demonstrated in Butcher et al. (2024), and updated for our new experiments, modelled surface velocity (Fig. 4E) in the standard run reaches maximum values (around 25×10^{-6} myr^{-1}) in the thickest, central area of the VFF, upstream of the major arcuate surface structures, with strong along-flow compression toward the terminus. Downstream of the structures, the calculated velocity decreases rapidly to very low values ($< 10^{-9}$ myr^{-1}). The ice-flow induced surface flux divergence results in small surface elevation changes (Fig. 4F) of $< \pm \sim 6 \times 10^{-6}$ myr^{-1} ($< \pm \sim 6$ m per Myr), which we correct for with the SEC (see Methods). Peak upward flow occurs in the zone of along-flow compression in the region of the arcuate surface structures, with peak downward flow (driven by along-flow extension) upstream of the structures, and especially upstream of the area of thickest ice and fastest flow in the northern part of the model domain. The gully also has an impact on the surface height change. Given that the gully post-dates the formation of the VFF and the arcuate surface structures (connected to VFF-internal layers) that it intersects, we only consider flow patterns >25 m north of the gully in subsequent analysis, where its influence diminishes.

Results for the sensitivity analysis of the flow exponent, ice temperature and ice grain size experiments are shown in Fig. 5. Fig. 5A shows the particle paths for 21 example seed particles which track to the upper (i.e. upflow), middle, and lower (downflow) arcuate VFF-surface structures (see Fig. 3) for the standard run. The particle paths remain very similar in all the sensitivity experiments, even for the different ice flow exponents. However, the calculated ice velocity, and therefore calculated age, varies markedly, especially for warmer ice and smaller inferred grain sizes, though almost all ages remain within the broad range of VFF ages inferred in the literature, i.e. Myr to 100 s Myr (e.g. Parsons et al., 2011; Fassett et al., 2014; Parsons and Holt, 2016; Conway et al., 2018; Baker and Carter, 2019; Hepburn et al., 2020; Berman et al., 2021; Butcher et al., 2021; Woodley et al., 2022).

The minimum, mean and maximum calculated ages of the particle paths emerging at the three arcuate surface structures are shown in Fig. 5B. This shows the strong dependence of the modelled age of ice on temperature; calculated ages for the 200 K and 230 K runs decrease by approximately two orders of magnitude for ice emerging at all three surface structures. Increasing grain size from 0.5 mm to 5 mm leads to an approximate 30 x increase in calculated ages, again across all three structures. The standard run, with $T_s = 210$ K and $n = 3$ produces ages between those for the $n = 2$, $d = 2$ mm and $n = 2$, $d = 5$ mm runs.

Fig. 6A shows the calculated surface age across the VFF surface from the full (4860 seed) particle track analysis, together with the calculated particle paths and depths for the 21 particles emerging along three of the major arcuate surface structures (as Fig. 5A) for the standard run. There is a clear and rapid increase in surface age toward the VFF terminus. The particle paths show that ice emerging at the lower arcuate structure has come from furthest upstream, and reaches greater depths in the VFF interior along its transport path. Thus, the calculated surface ages increase toward the VFF terminus, both due to longer transport distances along particle paths, and the decrease in calculated ice flow velocities as depth increases in the VFF (Fig. 3D). The calculated ages in upstream areas, especially where ice flow vectors trend downwards into the VFF (Fig. 4F), are young (< 1 Myr, or zero), though there is a small area of locally-higher ages (~ 20–40 Myr) just downstream of the crevassed area (Fig. 6A), where local flow compression leads to upward deflection of ice flow vectors from the VFF interior.

Fig. 6B shows the emergence locations for all seed particles where the path length exceeds 100 m, colour-coded by the seed particle source elevation. The main areas of emergence are in the vicinity of the arcuate surface structures, with ice emerging at lower elevations coming from higher elevations and further upstream. Seed particles emplaced very close to the headwall travel the furthest (shown bright yellow in Fig. 6B), emerging at or just down-ice from the lowest of the visible surface structures. There are also smaller areas of emergence in the lower part of the crevassed area, with particles emerging from near the headwall here, leading to the local area of relatively high surface ice ages (Fig. 6A).

Fig. 6C shows cross sections of the modelled age of ice, with the colour scale showing the modelled isochrons (effectively ice layers) for the transect cross sections, and particle paths (coloured lines) emerging at three of the arcuate surface structures for the two transects shown in Fig. 6B (a – a', Transect S; b – b', Transect N (compare with Fig. 2). Both show similar overall behaviour. Age increases with depth in the VFF,

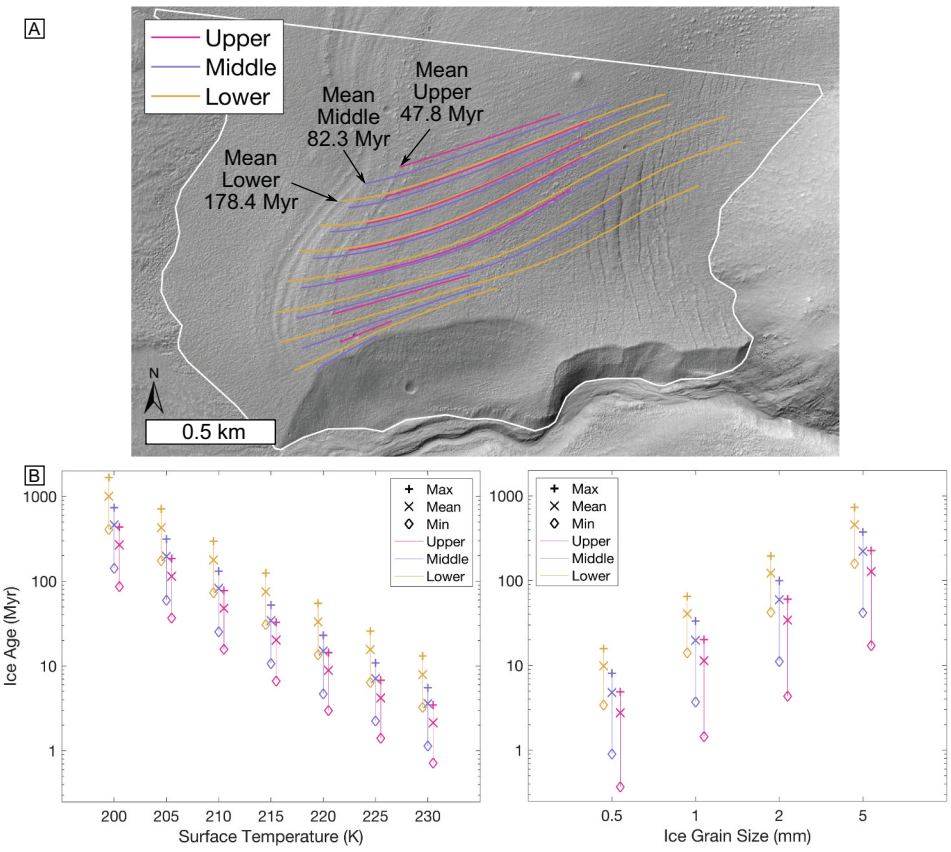

Fig. 5. Examples of modelled particle flow paths connecting to major arcuate structures on the VFF surface, and sensitivity of calculated particle transport durations (i.e. age of ice at emergence on the VFF surface) to surface temperature and ice grain size. (A) Particle flow paths for 21 example particles emerging along the Upper, Middle, and Lower arcuate surface structures, showing the mean age of ice where these paths emerge at each surface structure in the standard model run. Background image is orthorectified HiRISE image ESP_051036_1370_RED. (B) Sensitivity experiment results showing the calculated maximum, mean and minimum surface ice ages for particle paths emerging at the major arcuate surface structures shown in A. The left plot shows the n = 3, variable temperature experiments, and the right plot shows the n = 2, variable grain size experiments. For visual clarity, the results for particle paths emerging at the upper and lower structures are offset along the x axis from those of the middle structure; however, the temperatures and particles sizes are identical for each particular sensitivity experiment. HiRISE image credit: HiRISE data credit: NASA/JPL/University of Arizona/NHM.

and particles emerging nearer the terminus have come from furthest upstream and reach deeper into the VFF. Surface ice age increases rapidly toward the terminus, and the isochronous layers at depth become increasingly inclined toward the surface. The particle paths also show this change in vertical direction relative to the ice surface as they approach their emergence location. This is particularly marked for the isochrons and particles which emerge closest to the terminus, around the lower arcuate surface structure, which both show a strong change in direction in the final ~50 m of their path. The increase in angle qualitatively matches the changing dip measured by Butcher et al. (2024), and is consistent with observations from terrestrial glaciers, including cold-based, stratified, debris covered glaciers in Antarctica (e.g. Mackay and Marchant, 2017).

Table 2 gives the age of ice and particle path depths at the respective emergence points and at a W-E distance of 900 m from the VFF terminus (an arbitrary distance, where particle tracks are approximately surface and bed-parallel), for the particle paths shown in Fig. 6C. They show a clear age/depth relationship, with a rapid increase in age toward the bed, especially for Transect S.

As also seen in Fig. 6, no modelled long-distance particle transport paths reach the area of thin VFF materials between the arcuate surface structures and the VFF terminus due to the strong upwards tilting of flow within the VFF at the structures. This prevents the calculation of the age of ice in this area. We refer to this zone as the 'dynamically-detached zone' (Fig. 6A) because in the modelled stress and velocity fields, the strong compression and upwards flow in the area of the structures acts as a form of dynamic barrier, preventing ice from upstream reaching the very thin materials nearer the VFF terminus. Seed particles emplaced on the very shallow marginal area only travel very short distances, and very slowly, due to the very shallow ice in this area. They also typically do not move downward into the body of the ice in this area but are only carried short distances, at very shallow depths. We return to interpretation of this zone in the Discussion.

4. Discussion

Our results suggest that ice flow dynamics lead to systematic variations in the age of ice across VFFs (putative debris-covered glaciers) on Mars, consistent with variations observed in terrestrial glaciers. For the simple lobate VFF modelled here, and likely other such lobate VFFs on Mars, upstream areas have the youngest near-surface ice ages, and the age of near-surface ice increases rapidly toward the terminus. This age distribution is driven in large part by downward or upward movement of ice into or out of the VFF body caused by extensional or compressive ice flow in different areas of the VFF. With the exception of a very narrow, thin band of ice in the dynamically-detached zone immediately adjacent to the terminus (discussed later), the strong along-flow convergence toward the terminus (as driving stress decreases and ice velocity slows) leads to particle flow paths becoming inclined upward toward the surface near to the terminus. Ice emerging nearer the terminus has its source further upstream, and has reached greater depths within the VFF along its transport pathway. The longer particle path lengths, and the

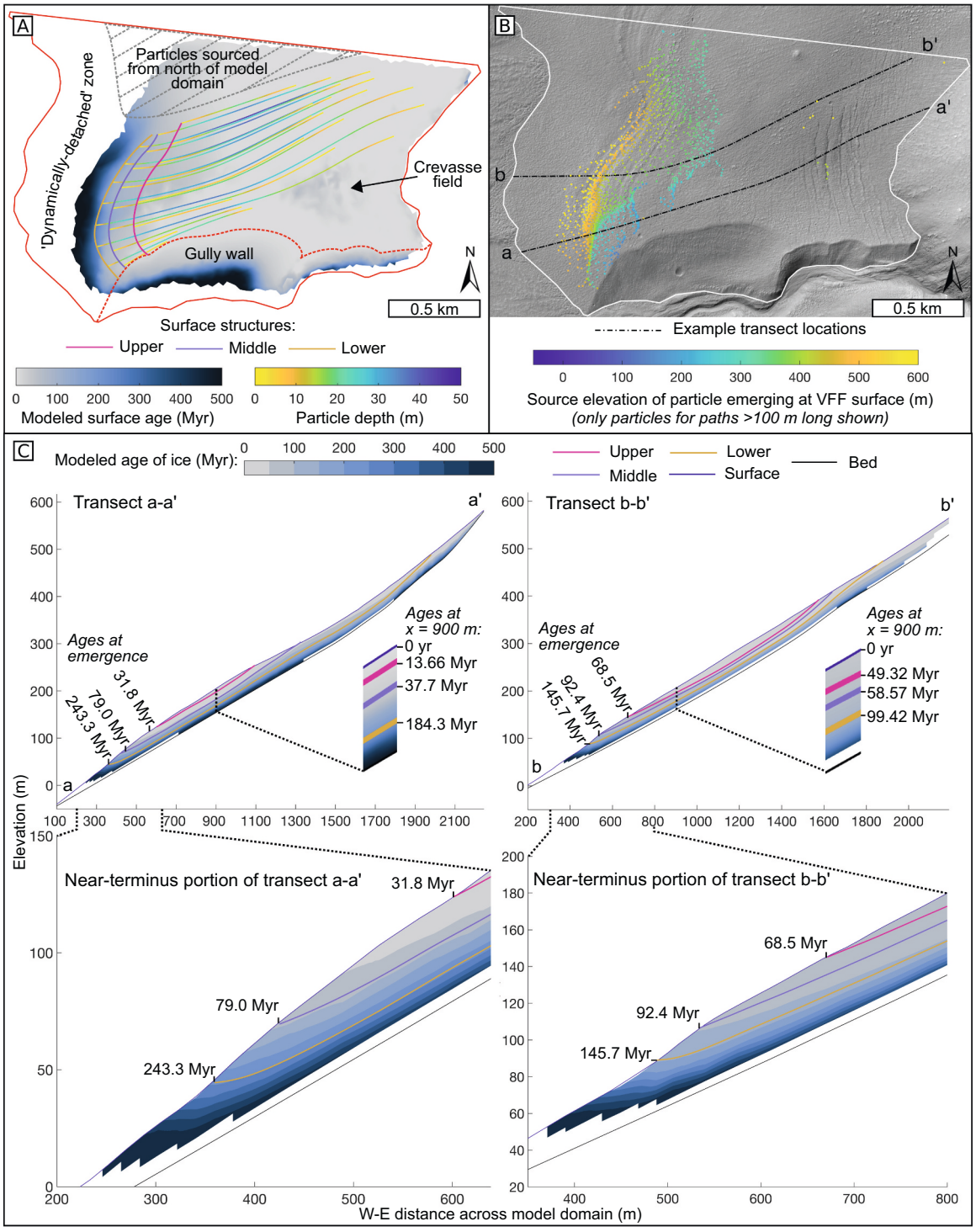

Fig. 6. Modelled variations in the age of ice across the VFF surface and with depth. (A) Map of ice-surface ages for the standard run, interpolated from the emergence ages of the 2314 particles shown in panel B. The depth of particles within the VFF are shown as colour variations along the 21 particle paths which emerge at the major arcuate surface structures (same paths as Fig. 5). The positions of the arcuate surface structures are shown and colour-coded as in Fig. 5. The full model domain is outlined in red; areas inside the model domain with no age information are areas where no particle paths longer than 100 m terminate, preventing age calculation. Hatched area shows the approximate portion of the model domain where particle paths emerging near the snout source from outside the northern edge of the model domain. (B) Seed particle emergence points used to calculate ages in panel A, colour-coded by the source elevation of the seed particle. Points are shown where the path length is >100 m, and particles emerging in the gully wall are excluded due to the effect of gully morphology on calculated flow close to (i.e. within ~25 m of) the gully. Dashed lines show the locations of transects a–a' and b–b' in panel C. Background image is orthorectified HiRISE image ESP_051036_1370_RED. (C) Modelled Ice age/depth profiles for transects a–a' and b–b' (locations in panel B). Overlain are example vertical flow paths for those particle paths closest to each transect which emerge at the upper, middle, and lower arcuate surface structures (colour-coded as in Figs. 5A). Zoomed portions (bottom row) show the area approaching the VFF terminus where the modelled flow paths are deflected up toward the surface. Ages from Table 2 are shown at the emergence points, and for a hypothetical vertical transect 900 m from the westernmost edge of the model domain at each transect. White areas within the model domain at the lowest levels, and at the terminus (as in A) are locations where no particle paths reach, preventing age calculation. HiRISE image credit: NASA/JPL/University of Arizona/NHM. (For interpretation of the references to colour in this figure legend, the reader is referred to the web version of this article.)

Table 2
Ice age/depth values extracted at x = 900 m along transects a-a' and b-b' (shown in Fig. 6C) and at the emergence points for the standard model run. Values correspond to particle paths which eventually emerge at the upper, middle, and lower surface structures further down-flow. For comparison, the mean ages of ice emerging at the major arcuate surface structures in the standard run for the 21 paths in Figs. 5A and 6A are: Upper: 47.8 Myr; Middle: 82.3 Myr; Lower: 178.4 Myr.

Location	Depth, x = 900 m (m)	Age, x = 900 m (Myr)	Age at emergence (Myr)
Transect S (a–a', Fig. 6C)			
Upper	8.32	13.66	31.8
Middle	16.62	37.7	79.0
Lower	35.41	184.3	243.3
Transect N (b-b' Fig. 6D)			
Upper	9.41	49.32	68.5
Middle	15.41	58.57	92.4
Lower	27.61	99.42	145.7

vertical velocity structure within the VFF (with velocity decreasing rapidly near the bed) therefore means ice emerging nearer the terminus is much older than ice outcropping upglacier, further from the terminus. Vertical profiles of the modelled age of ice (Fig. 6C) within the VFF also show the upward inclination of isochronous layers toward the surface approaching the terminus. This behaviour qualitatively matches observations by Butcher et al. (2024) of englacial structures which outcrop in the wall of the gully which incises through this particular VFF; the observed layers become increasingly tilted upwards from the bed approaching the VFF terminus and connect to major arcuate structures on the VFF surface (Butcher et al., 2024).

The modelled area of young ice across the upper parts of the VFF is similar to the rather young crater retention age (~2.7 Myr) reported in the region (Berman et al., 2021), but the ice-marginal surface ages we calculate here are much older. They are, however, at the lower end of crater retention age estimates (10s – 100 s Myr) for the broader population of VFFs on Mars, which are typically larger (10s km) and thicker (100 s m) than the VFF analysed here (Butcher et al., 2017).

The flow-induced variations we find in the calculated ages of near-surface ice in VFFs highlight the difficulty in using crater retention ages to obtain robust age information for glacial deposits on Mars which likely have undergone flow deformation, and in the mid-latitudes are buried by a later covering of dust/debris. Impact crater retention ages reflect the time since the impact crater population in the surface layer was last erased or significantly modified (i.e., by emplacement and/or later modification or resurfacing of the surface debris layer). While the stratigraphy of VFFs with respect to underlying geological units on Mars (e.g. Butcher et al., 2021; Conway et al., 2018; Tanaka et al., 2014; Woodley et al., 2022) demonstrates with high confidence that VFFs are geologically young (likely having formed within the last ~1 Gyr, during the mid-to-late Amazonian period), crater-retention ages from the surficial debris layers on VFFs themselves (typically ranging from a few Myr to hundreds of Myr) provide spatially uniform estimates of the minimum age of the underlying ice. They could significantly underestimate the specific emplacement ages of the ice layers beneath the surface, and are unable to provide information on the emplacement ages of different ice layers with depth, or variations in the age of ice where those layers outcrop near to the surface (below the surface debris layer). As predicted by theoretical glacial flow patterns, our model simulations show that VFF surface age could vary by several orders of magnitude across the VFF surface. The length scales over which variations in the age of near-surface ice occur are 10s to 100 s m, i.e. comparable to the diameters of individual impact craters on VFF surfaces.

The very clear spatial agreement between the major arcuate surface structures on the VFF and the modelled "dynamic limit", beyond which particle paths flowing from upstream toward the terminus cannot reach (Fig. 7a), suggests that the very shallow ice at the terminus of the VFF is dynamically detached from the main VFF body. This could reflect a degree of thinning or degradation of the original VFF in this area; a small amount of surface lowering (i.e., thinning) here would amount to a proportionally large loss of the total ice column thickness compared to thicker sections upflow, reducing modelled ice velocity markedly, and therefore the ability to reliably model past ice flow into this area. Alternatively, the materials beyond the modelled dynamic limit could be a later mantling deposit which has accumulated at the break of slope near the VFF terminus. The surface texture of this shallow apron is different to other portions of the VFF surface, and continuous with thin deposits in an alcove at the northern edge of the VFF that is disconnected from the main VFF body by a bedrock prominence. South of the gully which dissects the VFF, there is a small lobe (Fig. 7B) which may constitute the section of the VFF disconnected from the main ice mass by the gully. A topographic break in slope exists between this lobe and thin materials downslope which appear similar to those in the dynamically detached zone of the VFF (Fig. 7B). They are laterally continuous with thin deposits which mantle hillslopes to the south and which backfill arcuate moraine-like ridges (Fig. 7 A and 7C). These ridges are interpreted by Butcher et al. (2024) as controlled moraines i.e., ice-cored ridges tracing the locations of former englacial debris bands (see e.g. Evans, 2009) similar to those bands observed in the gully incision through the extant VFF. If these moraine-like ridges relate to a broadly similar phase of glaciation to the VFF, the backfilling of the ridges by the mantling deposits suggests that the thin materials at the VFF terminus may indeed be a later onlapping deposit (Fig. 7). However, further study is required to assess the origins of such materials, which are often observed at VFF termini.

The qualitative spatial patterns in the modelled age of ice, and the ice flow paths within the VFF, are repeated in all our experiments, including those where we use different flow exponents. However, the calculated ages themselves strongly vary with the inferred surface temperature and the assumed ice grain size. This suggests that factors affecting the ice hardness such as temperature and grain size emerge as the key unknowns affecting our calculated model ages, not the specific ice deformation mechanism(s) or the flow exponent. The temperature-flow rate-age sensitivity we find in particular suggests that Mars' highly variable orbital (and hence climatic) history could lead to a complex palimpsest of surface flow features and englacial layers, in which the flow signatures from multiple periods with faster ice flow due to increased accumulation (and hence thicker ice) and/or warmer climates, could "catch up with", and potentially over-ride, features formed in drier, colder, and hence slower-flow periods (Schmidt et al., 2019; Levy et al., 2021). Larger, more complex VFF systems have shown multiple phases of flow with smaller VFFs seeming to override or flow into larger ones (Hepburn et al., 2020); the temperature sensitivity of ice flow we find could suggest that such behaviour could be rather common, and could also occur in simple VFFs especially if they formed over multiple accumulation/ablation episodes (Levy et al., 2021).

Our results suggest that flow exponents (n) of either 2 or 3 can produce very similar surface age distributions and age-depth relationships depending on the inferred ice temperature and grain size. This finding bolsters the suggestion from previous modelling studies of larger VFFs, where the ice thickness is constrained from SHARAD radar sounding data (Seu et al., 2007), that differing ice flow mechanisms and flow exponents are equally capable of producing observed VFF morphologies with similar overall errors (Parsons et al., 2011; Karlsson et al., 2015; Parsons and Holt, 2016; Schmidt et al., 2019).

5. Conclusions and implications for future ice-access missions

We use ice flow physics and particle tracking to reconstruct ice 3D variations in the minimum age of ice within a small kilometre-scale VFF (putative debris-covered glacier) in the Nereidum region of Mars' southern mid-latitudes. The 3D age reconstructions are based on

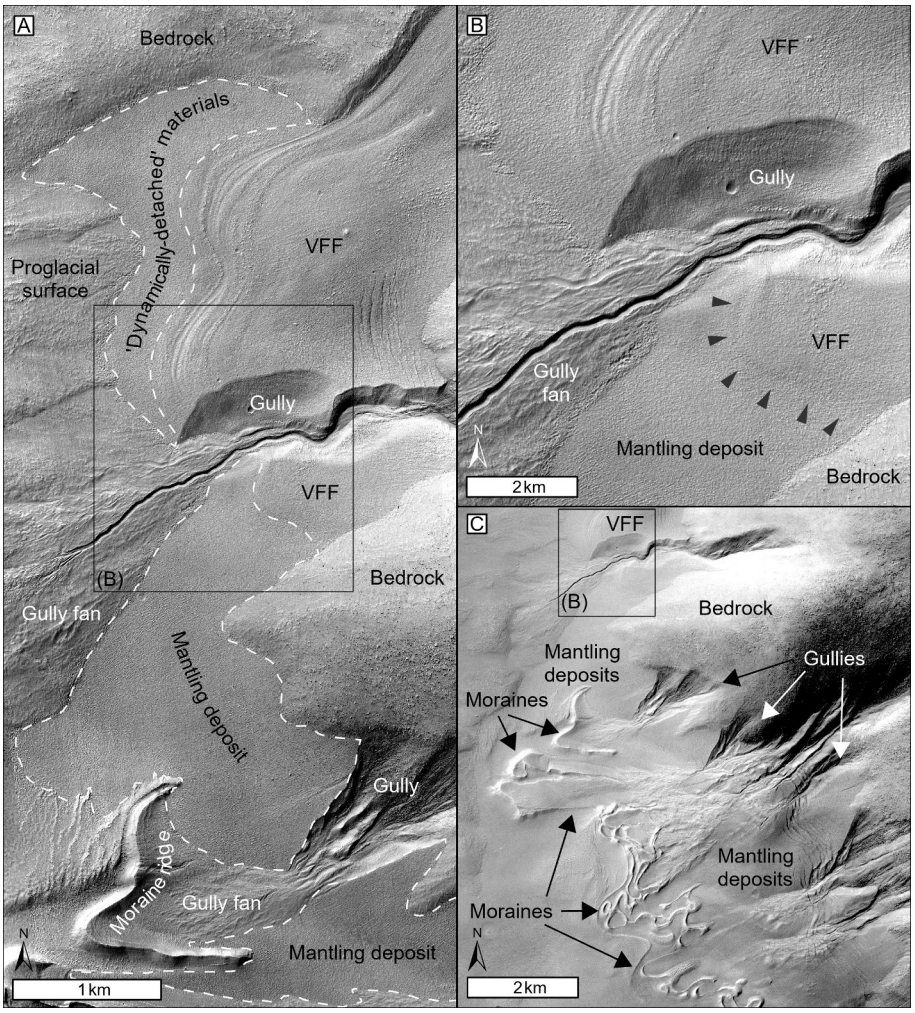

Fig. 7. Morphological context for the portion of the VFF beyond the major arcuate surface structures which model results suggest are 'dynamically detached' from the main VFF flow, and may instead represent younger materials draped over the VFF terminus and associated with young ice-rich mantling deposits on adjacent hillslopes. (A) HiRISE orthoimage ESP_051036_1370_RED showing the approximate extent of the dynamically-detached unit (into which no particle paths extend from further up-flow), including its inferred extent north of the model domain. Also shown is the extent of mantling deposits (likely ice-rich) on hillslopes to the south of the VFF. The black box shows the extent of panel B. (B) Zoom in on the VFF deposits either side of the gully incision (extent shown in A), showing the lobate topographic signature of a potential contact, or flow front (black arrows) between the southern part of the VFF (detached from the main VFF by later gully incision), and a mantling deposit which extends around the hillslope to the south. Same HiRISE image as A. (C) CTX image P14_006572_1367_XN_43S051W showing the embayment of lobate moraine ridges south of the VFF by mantling deposits on hillslopes, including the mantling deposit in contact with the VFF in B. If the moraines relate to a similar phase of glaciation to the VFF, this suggests the mantling deposits (and dynamically-detached unit) formed after the main phase of VFF accumulation and flow, and could therefore be younger in age. CTX data credit: NASA/JPL/MSSS/UfoA. HiRISE data credit: NASA/JPL/University of Arizona/NHM.

calculations of the transit times of ice particles through the VFF under steady state conditions. We investigate the impact on the calculated age distributions of two different ice deformation mechanisms, and of a range of mean annual surface temperatures and ice grain sizes for an assumed steady-state VFF morphology. Modelled surface ages increase significantly toward the terminus of the VFF, and over small distances, as the ice becomes thinner, and the resulting ice flow compression forces deep, old ice up toward the surface. We also find a smaller area of locally older ice in an upstream part of the VFF where flow local compression occurs. There is a strong gradient in the age of ice with depth throughout the VFF, with isochronous layers of ice becoming increasingly tilted upwards toward the VFF surface nearer to the terminus.

The spatial patterns in the relative age of near-surface ice across the VFF, and with depth through the ice column, are robust to the form and rate exponent of the flow law itself; instead, the ice temperature and grain size, driven by the assumed dust content (as controls on the ice rigidity, and hence flow velocity) emerge as the critical controls on flow rate, and hence the specific calculated ice age distribution.

Our results demonstrate a physically-based numerical ice-flow modelling approach for estimating – to the first order – the age of ice and its spatial variations across VFF surfaces and through the ice column. Our method acts as a valuable adjunct to impact crater retention age estimates, revealing areas of potentially younger and older ice created by ice flow dynamics over shorter spatial distances than is possible with impact crater counting methods. Our method forms a clear basis for future methodological developments to investigate (a) the likely influence of variable mass balance and climatic histories on VFF ages and the spatial complexities of intra-VFF age variations, and/or (b) the possible effects of englacial variations in lithic content or ice rheology, which may also occur if VFFs formed though multiple periods of accumulation/ablation (Levy et al., 2021; Parsons et al., 2020).

There is much focus upon mid-latitude ice deposits on Mars, including VFFs, as key targets for future orbital, robotic, and eventual human missions, including for the purposes of searching for microbial life and reconstructing Mars' climate history from ice core records (Mars Ice Core Working Group, 2021). As discussed by Butcher et al. (2024),

the outcropping of progressively older layers ice in the shallow subsurface close to VFF termini raises the possibility that future missions could take shallow samples in VFF-terminal zones to access older ice than may be possible with vertical coring alone, thereby extending the timespan of potential climate records (and other types of records preserved within glacial ice) that could be accessed and analysed with shallow ice coring. Our results illustrate that, even for a simple VFF modelled at assumed steady state, the age of near-surface ice varies significantly within an individual glacial system, as does the likely configuration and deformation history of internal, isochronous ice layers. The temperature sensitivity we find in particular suggests that the variability of martian climate conditions in its recent past could have had major impacts on the form of VFFs, making them a valuable source of information on Mars' climate history. Hence, the specific scientific questions which could be addressed by analysing and sampling ice in VFFs, including the timing and timespans (and preservation states) of accessible climate records, will depend on the specific locations from which those samples are extracted, and could vary over short distances. It is therefore essential when identifying potential landing sites and planning sampling strategies for future ice-sampling missions (either robotic or human-led), that detailed consideration is given to the effects of glacial processes on the science potential of ice sampled from different locations, including within individual glacial systems.

The method we have developed, and its results, also highlight a pressing need for new ice-penetrating radar data which resolves the internal layering structure of small ice masses such as VFFs on Mars, and their detailed bed topography (e.g. I-MIM MDT, 2022). The VFF we study here is unusual in many ways; the gully incised through it allowed arcuate surface structures in visible imagery to be linked to tilted englacial structures visible in the gully walls, which matched our modelled flow patterns. Perhaps more fundamentally, however, the presence of the gully enabled us to determine the VFF thickness in the region of the gully, and produce a DTM of the VFF based on the gully elevation and the surrounding ice margin with a reasonable degree of confidence. A number of VFF basal reflectors have been detected by the SHARAD sounding radar onboard the Mars Reconnaissance Orbiter mission (Seu et al., 2007), but these are limited to larger, flatter VFFs (specifically large, topographically unconfined 'lobate debris aprons'). Detection of englacial layers is also very challenging given the capability of the current instrument, though work here is ongoing (e.g. Aguilar et al., 2024; Perry et al., 2024). For most VFFs, however, the bed elevation (and hence precise ice thickness) is unknown. More systematic coverage of VFF beds, and the capability to detect layers within the ice, would help unlock Mars' complex glacial and climatic history, and underpin the success of any future ice sampling mission.

CRediT authorship contribution statement

N.S. Arnold: Conceptualization, Methodology, Software, Formal analysis, Investigation, Data curation, Writing – original draft, Writing – review & editing, Visualization. **F.E.G. Butcher:** Writing – review & editing, Visualization, Validation, Methodology, Investigation, Funding acquisition, Formal analysis, Conceptualization.

Declaration of competing interest

The authors declare that they have no known competing financial interests or personal relationships that could have appeared to influence the work reported in this paper.

Acknowledgements

NSA thanks the B.B. Roberts fund of the Scott Polar Research Institute, and St Johns College, Cambridge, for financial support to present this research at the 8th International Conference on Mars Polar Science and Exploration in Whitehorse, Canada (July 2024). FEGB acknowledges a Leverhulme Trust Early Career Research Fellowship (ECF-2022-025) and a UK Space Agency Exploration Science Fellowship (UKRI1370). We thank Mathieu Morlighem, and other members of the ISSM development team, for ongoing help and advice around the use of ISSM. We gratefully acknowledge the hard work of the teams who brought various Mars orbital missions to fruition, and who continue to deliver fascinating data such as that used in this study.

Data availability

Orbital datasets used herein are freely available from the NASA Planetary Data System at https://ode.rsl.wustl.edu/mars/. CTX images are available from the University of Arizona at http://viewer.mars.asu.edu/viewer/ctx, and HiRISE products are available from the HiRISE website at https://www.uahirise.org/. The HiRISE surface DTM and orthoimage we used (from Butcher et al., 2024) are available at https://doi.org/10.15131/shef.data.23741973.v1. The VFF bed DTM and particle tracking code we generated for this study are available at: https://doi.org/10.17863/CAM.121956. The Ice Sheet and Sea Level System Model (ISSM) used herein is available at: https://issm.jpl.nasa.gov/.

References

Aguilar, R., Nerozzi, S., Christoffersen, M.S., Holt, J.W., 2024. New insights on internal layering of Martian mid-latitude glaciers with SHARAD. In: In: 8th International Conference on Mars Polar Science and Exploration. Lunar and Planetary Institute, Houston p. Abstract #6064.

Anderson, R.S., Anderson, L.S., Armstrong, W.H., Rossi, M.W., Crump, S.E., 2018. Glaciation of alpine valleys: the glacier – debris-covered glacier – rock glacier continuum. Geomorphology 311, 127–142. https://doi.org/10.1016/j.geomorph.2018.03.015.

Arnold, N.S., Butcher, F.E.G., Conway, S.J., Gallagher, C., Balme, M.R., 2022. Surface topographic impact of subglacial water beneath the south polar ice cap of Mars. Nat Astron 6, 1256–1262. https://doi.org/10.1038/s41550-022-01782-0.

Baker, D.M.H., Carter, L.M., 2019. Probing supraglacial debris on Mars 2: crater morphology. Icarus 319, 264–280. https://doi.org/10.1016/j.icarus.2018.09.009.

Barr, A.C., Milkovich, S.M., 2008. Ice grain size and the rheology of the martian polar deposits. Icarus 194, 513–518. https://doi.org/10.1016/j.icarus.2007.11.018.

Berman, D.C., Chuang, F.C., Smith, I.B., Crown, D.A., 2021. Ice-rich landforms of the southern mid-latitudes of mars: a case study in Nereidum Montes. Icarus 355, 114170. https://doi.org/10.1016/j.icarus.2020.114170.

Blatter, H., 1995. Velocity and stress fields in grounded glaciers: a simple algorithm for including deviatoric stress gradients. J. Glaciol. 41, 333–344. https://doi.org/10.3189/S002214300001621X.

Brook, E., Center for Oldest Ice Exploration Allan Hills Research Team, 2025. Plio-Pleistocene ice cores from the Allan Hills blue ice area. In: Antarctica: Recent Results and Prospects for Future Work. https://doi.org/10.5194/egusphere-egu24-4497.

Butcher, F.E.G., Balme, M.R., Gallagher, C., Arnold, N.S., Conway, S.J., Hagermann, A., Lewis, S.R., 2017. Recent basal melting of a mid-latitude glacier on Mars. J. Geophys. Res. Planets 122, 2445–2468. https://doi.org/10.1002/2017JE005434.

Butcher, F.E.G., Balme, M.R., Conway, S.J., Gallagher, C., Arnold, N.S., Storrar, R.D., Lewis, S.R., Hagermann, A., Davis, J.M., 2021. Sinuous ridges in Chukhung crater, Tempe Terra, Mars: implications for fluvial, glacial, and glaciofluvial activity. Icarus 357, 114131. https://doi.org/10.1016/j.icarus.2020.114131.

Butcher, F.E.G., Arnold, N.S., Conway, S.J., Berman, D.C., Davis, J.M., Balme, M.R., 2024. The internal structure of a debris-covered glacier on Mars revealed by gully incision. Icarus 419, 115717. https://doi.org/10.1016/j.icarus.2023.115717.

Conway, S.J., Butcher, F.E.G., de Haas, T., Deijns, A.A.J., Grindrod, P.M., Davis, J.M., 2018. Glacial and gully erosion on Mars: a terrestrial perspective. Geomorphology 318, 26–57. https://doi.org/10.1016/j.geomorph.2018.05.019.

Cuffey, K., Paterson, W.S.B., 2010. The Physics of Glaciers, 4th ed. Butterworth-Heinemann/Elsevier, Burlington, MA.

Das, I., Bell, R.E., Scambos, T.A., Wolovick, M., Creyts, T.T., Studinger, M., Frearson, N., Nicolas, J.P., Lenaerts, J.T.M., Van Den Broeke, M.R., 2013. Influence of persistent wind scour on the surface mass balance of Antarctica. Nat. Geosci. 6, 367–371. https://doi.org/10.1038/ngeo1766.

Evans, D.J.A., 2009. Controlled moraines: origins, characteristics and palaeoglaciological implications. Quat. Sci. Rev. 28, 183–208. https://doi.org/10.1016/j.quascirev.2008.10.024.

Fassett, C.I., Levy, J.S., Dickson, J.L., Head, J.W., 2014. An extended period of episodic northern mid-latitude glaciation on Mars during the middle to late Amazonian: implications for long-term obliquity history. Geology 42, 763–766. https://doi.org/10.1130/G35798.1.

Fastook, J.L., Head, J.W., 2024. Modeling glaciation of the Hellas Basin, Mars, for a 'cold and icy' late Noachian Paleoclimatic scenario. Icarus 421, 116222. https://doi.org/10.1016/j.icarus.2024.116222.

Fischer, H., Severinghaus, J., Brook, E., Wolff, E., Albert, M., Alemany, O., Arthern, R., Bentley, C., Blankenship, D., Chappellaz, J., Creyts, T., Dahl-Jensen, D., Dinn, M.,

Frezzotti, M., Fujita, S., Gallee, H., Hindmarsh, R., Hudspeth, D., Jugie, G., Kawamura, K., Lipenkov, V., Miller, H., Mulvaney, R., Parrenin, F., Pattyn, F., Ritz, C., Schwander, J., Steinhage, D., Van Ommen, T., Wilhelms, F., 2013. Where to find 1.5 million yr old ice for the IPICS "oldest-ice" ice core. Clim. Past 9, 2489–2505. https://doi.org/10.5194/cp-9-2489-2013.

Frezzotti, M., Pourchet, M., Flora, O., Gandolfi, S., Gay, M., Urbini, S., Vincent, C., Becagli, S., Gragnani, R., Proposito, M., Severi, M., Traversi, R., Udisti, R., Fily, M., 2004. New estimations of precipitation and surface sublimation in East Antarctica from snow accumulation measurements. Clim. Dyn. 23, 803–813. https://doi.org/10.1007/s00382-004-0462-5.

Glen, J.W., 1955. The creep of polycrystalline ice. Proceedings of the Royal Society of London. Ser. A, Math. Phys. Sci. 228, 519–538.

Goldsby, D.L., Kohlstedt, D.L., 2001. Superplastic deformation of ice: experimental observations. J. Geophys. Res. Solid Earth 106, 11017–11030. https://doi.org/10.1029/2000JB900336.

Hanna, E., Navarro, F.J., Pattyn, F., Domingues, C.M., Fettweis, X., Ivins, E.R., Nicholls, R.J., Ritz, C., Smith, B., Tulaczyk, S., Whitehouse, P.L., Zwally, H.J., 2013. Ice-sheet mass balance and climate change. Nature 498, 51–59. https://doi.org/10.1038/nature12238.

Hepburn, A.J., Ng, F.S.L., Livingstone, S.J., Holt, T.O., Hubbard, B., 2020. Polyphase mid-latitude glaciation on Mars: chronology of the formation of superposed glacier-like forms from crater-count dating. JGR Planets 125, e2019JE006102. https://doi.org/10.1029/2019JE006102.

Holt, J.W., Safaeinili, A., Plaut, J.J., Head, J.W., Phillips, R.J., Seu, R., Kempf, S.D., Choudhary, P., Young, D.A., Putzig, N.E., Biccari, D., Gim, Y., 2008. Radar sounding evidence for buried glaciers in the southern mid-latitudes of Mars. Science 322, 1235–1238. https://doi.org/10.1126/science.1164246.

Hooke, R.LeB, Hudleston, P.J., 1978. Origin of foliation in glaciers. J. Glaciol. 20, 285–299. https://doi.org/10.3189/S0022143000013848.

Hutter, K., 1983. Theoretical Glaciology. Theoretical glaciology /. Reidel.

I-MIM MDT, I., 2022. Final report of the international Mars ice mapper reconnaissance. Sci. Measur. Def. Team 239.

Jennings, S.J.A., Hambrey, M.J., 2021. Structures and deformation in glaciers and ice sheets. Rev. Geophys. 59, e2021RG000743. https://doi.org/10.1029/2021RG000743.

Karlsson, N.B., Schmidt, L.S., Hvidberg, C.S., 2015. Volume of Martian midlatitude glaciers from radar observations and ice flow modeling. Geophys. Res. Lett. 42, 2627–2633. https://doi.org/10.1002/2015GL063219.

Larour, E., Seroussi, H., Morlighem, M., Rignot, E., 2012. Continental scale, high order, high spatial resolution, ice sheet modeling using the ice sheet system model (ISSM). J. Geophys. Res. 117, 2011JF002140. https://doi.org/10.1029/2011JF002140.

Laskar, J., Correia, A.C.M., Gastineau, M., Joutel, F., Levrard, B., Robutel, P., 2004. Long term evolution and chaotic diffusion of the insolation quantities of Mars. Icarus 170, 343–364. https://doi.org/10.1016/j.icarus.2004.04.005.

Levy, J.S., Fassett, C.I., Holt, J.W., Parsons, R., Cipolli, W., Goudge, T.A., Tebolt, M., Kuentz, L., Johnson, J., Ishraque, F., Cvijanovich, B., Armstrong, I., 2021. Surface boulder banding indicates Martian debris-covered glaciers formed over multiple glaciations. Proc. Natl. Acad. Sci. 118, e2015971118. https://doi.org/10.1073/pnas.2015971118.

MacGregor, J.A., Fahnestock, M.A., Colgan, W.T., Larsen, N.K., Kjeldsen, K.K., Welker, J. M., 2020. The age of surface-exposed ice along the northern margin of the Greenland ice sheet. J. Glaciol. 66, 667–684. https://doi.org/10.1017/jog.2020.62.

Mackay, S.L., Marchant, D.R., 2017. Obliquity-paced climate change recorded in Antarctic debris-covered glaciers. Nat. Commun. 8, 14194. https://doi.org/10.1038/ncomms14194.

Madeleine, J.-B., Forget, F., Head, J.W., Levrard, B., Montmessin, F., Millour, E., 2009. Amazonian northern mid-latitude glaciation on Mars: a proposed climate scenario. Icarus 203, 390–405. https://doi.org/10.1016/j.icarus.2009.04.037.

Malin, M.C., Bell, J.F., Cantor, B.A., Caplinger, M.A., Calvin, W.M., Clancy, R.T., Edgett, K.S., Edwards, L., Haberle, R.M., James, P.B., Lee, S.W., Ravine, M.A., Thomas, P.C., Wolff, M.J., 2007. Context Camera Investigation on board the Mars Reconnaissance Orbiter. J. Geophys. Res. 112, 2006JE002808. https://doi.org/10.1029/2006JE002808.

Mars Ice Core Working Group, 2021. First Ice Cores from Mars, First Ice Cores from Mars. co-chairs: M.R. Albert and M. Koutnik. NASA.

McEwen, A.S., Eliason, E.M., Bergstrom, J.W., Bridges, N.T., Hansen, C.J., Delamere, W. A., Grant, J.A., Gulick, V.C., Herkenhoff, K.E., Keszthelyi, L., Kirk, R.L., Mellon, M.T., Squyres, S.W., Thomas, N., Weitz, C.M., 2007. Mars reconnaissance orbiter's high resolution imaging science experiment (HiRISE). J. Geophys. Res. 112, 2005JE002605. https://doi.org/10.1029/2005JE002605.

Milliken, R.E., Mustard, J.F., Goldsby, D.L., 2003. Viscous flow features on the surface of Mars: observations from high-resolution Mars orbiter camera (MOC) images. J. Geophys. Res. Planets 108. https://doi.org/10.1029/2002JE002005.

Millour, E., Forget, F., Spiga, A., Vals, M., Zakharov, V., Montabone, L., Lefèvre, F., Montmessin, F., Read, P.L., 2018. THE MARS CLIMATE DATABASE (VERSION 5.3). Presented at THE Scientific Workshop: From Mars Express to ExoMars.

Morgan, G.A., Putzig, N.E., Perry, M.R., Sizemore, H.G., Bramson, A.M., Petersen, E.I., Bain, Z.M., Baker, D.M.H., Mastrogiuseppe, M., Hoover, R.H., Smith, I.B., Pathare, A., Dundas, C.M., Campbell, B.A., 2021. Availability of subsurface water-ice resources in the northern mid-latitudes of Mars. Nat Astron 5, 230–236. https://doi.org/10.1038/s41550-020-01290-z.

Morgan, G.A., Putzig, N.E., Baker, D.M.H., Pathare, A., Dundas, C.M., Russell, M.B., Perry, M.R., Chojnacki, M., Sizemore, H.G., Bramson, A.M., Petersen, E.I., Nerozzi, S., Hoover, R.H., Bain, Z., 2025. Refined mapping of subsurface water ice on Mars to support future missions. Planet. Sci. J. 6, 29. https://doi.org/10.3847/PSJ/ad9b24.

National Academies of Sciences, E., and Medicine, 2023. Origins, Worlds, and Life: A Decadal Strategy for Planetary Science and Astrobiology 2023-2032. The National Academies Press, Washington, DC. https://doi.org/10.17226/26522.

Parsons, R., Holt, J., 2016. Constraints on the formation and properties of a Martian lobate debris apron: insights from high-resolution topography, SHARAD radar data, and a numerical ice flow model. J. Geophys. Res. Planets 121, 432–453. https://doi.org/10.1002/2015JE004927.

Parsons, R.A., Kanzaki, T., Hemmi, R., Miyamoto, H., 2020. Cold-based glaciation of Pavonis Mons, Mars: evidence for moraine deposition during glacial advance. Prog. earth planet. sci. 7 (1), 13. https://doi.org/10.1186/s40645-020-0323-9.

Parsons, R.A., Nimmo, F., Miyamoto, H., 2011. Constraints on martian lobate debris apron evolution and rheology from numerical modeling of ice flow. Icarus 214, 246–257. https://doi.org/10.1016/j.icarus.2011.04.014.

Pattyn, F., 2003. A new three-dimensional higher-order thermomechanical ice sheet model: basic sensitivity, ice stream development, and ice flow across subglacial lakes. J. Geophys. Res. 108, 2002JB002329. https://doi.org/10.1029/2002JB002329.

Perry, M.R., Russell, A.T., Russell, M.B., Foss, F.J., Chuang, F.C., Morgan, G.A., Bain, Z. M., Campbell, B.A., Putzig, N.E., 2024. Three-dimensional imaging of martian glaciated terrain using Mars reconnaissance orbiter shallow radar (SHARAD) observations. Icarus 419, 115716. https://doi.org/10.1016/j.icarus.2023.115716.

Petersen, E.I., Holt, J.W., Levy, J.S., 2018. High ice purity of Martian lobate debris aprons at the regional scale: evidence from an orbital radar sounding survey in Deuteronilus and Protonilus Mensae. Geophys. Res. Lett. 45. https://doi.org/10.1029/2018GL079759.

Plaut, J.J., Safaeinili, A., Holt, J.W., Phillips, R.J., Head, J.W., Seu, R., Putzig, N.E., Frigeri, A., 2009. Radar evidence for ice in lobate debris aprons in the mid-northern latitudes of Mars. Geophys. Res. Lett. 36, 2008GL036379. https://doi.org/10.1029/2008GL036379.

Rückamp, M., Kleiner, T., Humbert, A., 2022. Comparison of ice dynamics using full-Stokes and Blatter–Pattyn approximation: application to the Northeast Greenland Ice Stream. Cryosphere 16, 1675–1696. https://doi.org/10.5194/tc-16-1675-2022.

Scambos, T.A., Frezzotti, M., Haran, T., Bohlander, J., Lenaerts, J.T.M., Van Den Broeke, M.R., Jezek, K., Long, D., Urbini, S., Farness, K., Neumann, T., Albert, M., Winther, J.-G., 2012. Extent of low-accumulation "wind glaze" areas on the East Antarctic plateau: implications for continental ice mass balance. J. Glaciol. 58, 633–647. https://doi.org/10.3189/2012JoG11J232.

Schaefer, H., Petrenko, V.V., Brook, E.J., Severinghaus, J.P., Reeh, N., Melton, J.R., Mitchell, L., 2009. Ice stratigraphy at the Pâkitsoq ice margin, West Greenland, derived from gas records. J. Glaciol. 55, 411–421. https://doi.org/10.3189/002214309788816704.

Schmidt, L.S., Hvidberg, C.S., Kim, J.R., Karlsson, N.B., 2019. Non-linear flow modelling of a Martian lobate debris apron. J. Glaciol. 65, 889–899. https://doi.org/10.1017/jog.2019.54.

Seu, R., Phillips, R.J., Biccari, D., Orosei, R., Masdea, A., Picardi, G., Safaeinili, A., Campbell, B.A., Plaut, J.J., Marinangeli, L., Smrekar, S.E., Nunes, D.C., 2007. SHARAD sounding radar on the Mars reconnaissance orbiter. J. Geophys. Res. 112, 2006JE002745. https://doi.org/10.1029/2006JE002745.

Smith, D.E., Zuber, M.T., Frey, H.V., Garvin, J.B., Head, J.W., Muhleman, D.O., Pettengill, G.H., Phillips, R.J., Solomon, S.C., Zwally, H.J., Banerdt, W.B., Duxbury, T.C., Golombek, M.P., Lemoine, F.G., Neumann, G.A., Rowlands, D.D., Aharonson, O., Ford, P.G., Ivanov, A.B., Johnson, C.L., McGovern, P.J., Abshire, J.B., Afzal, R.S., Sun, X., 2001. Mars orbiter laser altimeter: experiment summary after the first year of global mapping of Mars. J. Geophys. Res. Planets 106, 23689–23722. https://doi.org/10.1029/2000JE001364.

Sori, M.M., Bramson, A.M., 2019. Water on Mars, with a grain of salt: local heat anomalies are required for basal melting of ice at the south pole today. Geophys. Res. Lett. 46, 1222–1231. https://doi.org/10.1029/2018GL080985.

Souness, C., Hubbard, B., Milliken, R.E., Quincey, D., 2012. An inventory and population-scale analysis of martian glacier-like forms. Icarus 217, 243–255. https://doi.org/10.1016/j.icarus.2011.10.020.

Tanaka, K.L., Skinner, J.A., Dohm, J.M., Irwin III, R.P., Kolb, E.J., Fortezzo, C.M., Platz, T., Michael, G.G., Hare, T.M., 2014. Geologic map of Mars (USGS Numbered Series No. 3292). Scientific Investigations Map. U.S. Geological Survey, Reston, VA.

Williams, A., 2021. Mars Life Explorer Mission Concept Study Report.

Woodley, S.Z., Butcher, F.E.G., Fawdon, P., Clark, C.D., Ng, F.S.L., Davis, J.M., Gallagher, C., 2022. Multiple sites of recent wet-based glaciation identified from eskers in western Tempe Terra, Mars. Icarus 386, 115147. https://doi.org/10.1016/j.icarus.2022.115147.